

Seismic monitoring of oil production: A feasibility study

D. Lumley¹, A. Nur², S. Strandenes³, J. Dvorkin², J. Packwood^{2 1}

ABSTRACT

We perform a feasibility study on the likelihood of seismically detecting and interpreting the time-varying changes in a North Sea reservoir during solution-gas-drive oil production from a horizontal well. This study integrates reservoir engineering fluid-flow simulations, rock physics measurements and transformations, and prestack seismic modeling and migration on a real but anonymous North Sea reservoir model. We calculate spatial distributions of reservoir rock properties from the fluid-flow simulation data, and map the associated seismic responses at three production-time snapshots: prior to any oil production (Base Survey), after 56 days (Monitor 1), and after 113 days (Monitor 2) of oil production. Multi-offset seismic surveys are simulated for each of these three production times. Using realistic seismic acquisition parameters, we are able to successfully detect and monitor dynamic gascap expansion in the reservoir during the fluid-flow simulation of the oil production process. Evidence of gas coning is clearly visible in the prestack-migrated difference sections at realistic seismic noise levels and frequency bandwidth.

INTRODUCTION

Hydrocarbon reservoirs are increasingly recognized as spatially heterogeneous entities in terms of pore-fluid content, pore-fluid saturation, porosity, permeability, lithology, and structural control. Knowledge of these reservoir parameters and their spatial variation is critical in the evaluation of the total volume of hydrocarbon reserves in place, in understanding and predicting physical processes in the reservoir such as fluid flow and heat transfer, and in projecting and monitoring reservoir fluid production and recovery as a function of time. A new diagnostic role for seismic has recently been proposed, in which several repeat seismic surveys are acquired in time-lapse mode to monitor reservoir production fluid-flow processes (e.g., Nur, 1989). This concept offers a method for better characterization of reservoir complexity by monitoring the flow of fluids with time in a producing reservoir. Additionally, 3-D seismic

¹ **email:** not available

¹ Stanford Exploration Project.

² Stanford Rock Physics Lab.

³ Norsk Hydro, Bergen, Norway.

monitoring may provide a full reservoir volume analysis of production sweep efficiency, early breakthrough prediction, and location of bypassed (unproduced) hydrocarbons. Seismic monitoring of reservoir production processes potentially offers a new dimension to the manner in which hydrocarbon reservoirs are currently developed and produced.

Previous work

Although the concept of time-lapse seismic reservoir monitoring is relatively recent, a few notable pilot projects have been attempted. Pullin et al. (1987) collected two 3-D seismic surveys before and after a steam pilot at an Athabasca tar sands reservoir site. By comparing time delay and amplitude attenuation maps between the two stacked surveys, they seemed to be able to qualitatively map the location of heated versus unheated zones. Their observed vertical time delays and amplitude attenuations through heated sections of the reservoir compared reasonable well with prior rock physics laboratory studies of the predicted thermal effects on seismic data. Eastwood et al. (1994) performed a similar analysis on a 3-D seismic monitor of an Alberta cyclic steam stimulation. Greaves and Fulp (1987) designed and analyzed a 3-D seismic monitoring experiment of an in situ combustion (fireflood) enhanced oil recovery (EOR) process. They collected three 3-D surface seismic datasets: one before combustion, and two during combustion. They made stacked sections from each survey and computed traveltimes and amplitude difference maps comparing each fireflood data set to the pre-fire base survey. They were able to monitor the volume of combustion burn accurately, as well as the sweep efficiency, with confirmation by pre- and post-burn borehole measurements. More recently, Graebner (1993) presented results of a 3-D marine seismic monitoring survey in the Oseberg field offshore Norway. The objective was to monitor the movement of the gascap over time during production. They compared reservoir fluid-flow simulation predictions of the gas-oil contact movement to the actual seismic observations, and found a weak seismic amplitude anomaly that partially correlated with the fluid-flow simulation data. They state that their results were inconclusive due to significant noise in the final seismic difference sections, and concerns about calibrating relative and absolute positioning errors between surveys.

Current research

In this paper, we present what we believe to be a major step forward in establishing the petrophysical basis for seismic reservoir monitoring, by conducting a comprehensive physical modeling study that integrates fluid-flow simulation and rock physics with seismic modeling and migration. We demonstrate the potential feasibility of performing seismic reservoir monitoring with a North Sea reservoir case study. Fluid-flow simulations were computed by Norsk Hydro for the case of solution-gas-drive oil production from a horizontal well in the reservoir after 56 and 113 days of production. Reservoir geology and core data measurements were combined to make rock physics transformations of the fluid-flow saturation, pressure and temperature data to seismic velocities and densities. Multi-offset elastic reflection seismogram surveys were simulated at each production phase. Prestack migration images clearly show gas coning during production for reasonable seismic noise levels and frequency bandwidth. Our

feasibility study may help reduce the financial risk associated with designing and implementing a seismic monitoring project given a pre-monitor engineering and petrophysical reservoir database.

FLUID-FLOW SIMULATION

The reservoir in this study is located within a large oil and gas field in the North Sea. The oil zone is at a depth of approximately 1500 meters, and it varies in thickness from a few meters to more than 20 meters. Horizontal drilling technology makes it possible to commercially produce oil from this thin oil zone. A horizontal well penetrates this oil zone in the center of the simulation grid, and is perforated along the borehole for a length of a few hundred meters. Norsk Hydro provided fluid-flow simulations of primary oil production from a horizontal well in the reservoir. The timeframe of the two simulation datasets was 56 and 113 days into production.

Reservoir properties

The productive interval of the reservoir consists of loosely consolidated sands with porosities ranging from 23% to 35%. Figure ?? shows the distribution of porosity in the reservoir on the simulation grid. All three fluid phases of gas, oil and water are simultaneously present. The reservoir oil is fairly heavy with a low gas-to-oil ratio of about 60. Typical values for the oil at reservoir conditions are: density 0.8 g/cc, bulk modulus 1020 MPa, viscosity 1.5 to 2.0 cp. The temperature in the reservoir is approximately uniform and constant at 60 °C. The overburden pressure is approximately 34 MPa and the pore pressure is about 16 MPa.

Simulation grid

The reservoir grid consists of 312 individual blocks, as schematically diagrammed in Figure ???. Figure ?? shows an expanded section of the reservoir grid in zone A. This irregular simulation grid ranges in depth intervals of one to tens of meters, and lateral intervals of tens to hundreds of meters. The grid covers a reservoir zone 45 m thick, comprised of 24 layers. The maximum structural dip along the reservoir is about 6° at the right end which is truncated by 40 m of fault throw. At both production times of 56 and 113 days, each grid cell was provided with a fluid-flow simulation data value of pore pressure, gas saturation, oil saturation, and water saturation. Temperature remained constant throughout the simulation.

Pore pressure

Pore pressure was calculated in the fluid-flow simulations for 56 and 113 days (Monitors 1 and 2) of solution-gas-drive oil production from the horizontal well, and at the initial Base survey state. The largest change in pore pressure during 113 days of simulated production is only



Figure 1: Porosity distribution in the reservoir, ranging from 23% (black) to 35% (white).



Figure 2: The reservoir fluid-flow simulation grid. Grid coordinates are shifted 750 m laterally compared to physical coordinates.



Figure 3: An expanded section “A” of the reservoir fluid-flow simulation grid. Grid coordinates are shifted 750 m laterally compared to physical coordinates.

–0.24 MPa (–35 psi), which is negligible in terms of velocity effect as shown in Figure ???. Figures ?? and ?? show the changes in reservoir pressure of the Monitor 1 and 2 simulations compared to the initial reservoir conditions. The diffusive decrease in reservoir pressure is associated with the withdrawal of oil from the vicinity of the horizontal wellbore, which is located at about 1560 m depth, and between 1.5–2.0 km distance in the coordinates of Figure ???. The well is perforated with increased density to the right, which explains the asymmetry of the pressure decrease during drawdown.

Oil saturation

Figure ?? shows the initial oil saturation state in the reservoir. The main oil zone is about 20 m thick at a depth of 1550 m and has a maximum saturation value of 90%. Figures ?? and ?? show the oil saturation distribution after 56 and 113 days of solution-gas drive respectively. These plots show the oil zone being pinched out rapidly by gascap expansion from above, and aquifer upwelling from below. This is usually indicative that the production rate is too fast to maintain a stable oil zone. Figures ?? and ?? show the changes in oil saturation from the initial state to 56 and 113 days of production. The pinchout due to gascap expansion and aquifer coning is clearly evident, as well as a slight overall downward migration of the entire oil zone due to the gas expanding above.

Water saturation

Figure ?? shows the initial water saturation state in the reservoir. A large aquifer underlays the oil zone, and the oil-water contact follows reservoir structure and porosity rather than a gravity fluid contact. Figures ?? and ?? show the water saturation distribution after 56 and



Figure 4: Pore pressure difference: 56 days – initial state. All pressure changes are negative. The maximum change is about -0.16 MPa (dark gray).



Figure 5: Pore pressure difference: 113 days – initial state. All pressure changes are negative. The maximum change is about -0.24 MPa (black).



Figure 6: The initial oil saturation distribution. 100% saturation is white, 0% saturation is black.



Figure 7: The oil saturation distribution after 56 days of production. 100% saturation is white, 0% saturation is black.



Figure 8: The oil saturation distribution after 56 days of production. 100% saturation is white, 0% saturation is black.



Figure 9: The change in oil saturation: 56 days – initial state. +100% is white, –100% is black.



Figure 10: The change in oil saturation: 113 days – initial state. +100% is white, –100% is black.

113 days of solution-gas drive respectively. Note the aquifer coning upward in the center and the gravity sag at the flanks of the aquifer cone. Figures ?? and ?? show the changes in water saturation from the initial state to 56 and 113 days of production. The aquifer has coned upward near the horizontal wellbore to displace oil into production. Gravitational forces cause a slight downwelling of the aquifer at the flanks to balance the upward coning in the center.

Gas saturation

Figure ?? shows the initial gas saturation state in the reservoir. A 50 m thick gascap overlays the oil zone, and is sealed at the top by an impermeable cap rock. Figures ?? and ?? show the gas saturation distribution after 56 and 113 days of solution-gas drive respectively. Note the gascap coning downward in the center due to gas expansion associated with the reservoir pressure decrease. Figures ?? and ?? show the changes in gas saturation from the initial state to 56 and 113 days of production. The gascap has coned downward near the horizontal wellbore to displace oil into production. Since the compressibility of gas is orders of magnitude larger than that of water, the gascap cones downward more than the aquifer cones upward. The large gascap expansion is the primary production mechanism for solution-gas drive. Since a large P-impedance contrast is associated with the gas zone, we expect to see a seismic response to the gascap coning, as demonstrated later in this paper.



Figure 11: The initial water saturation distribution. 100% saturation is white, 0% saturation is black.



Figure 12: The water saturation distribution after 56 days of production. 100% saturation is white, 0% saturation is black.



Figure 13: The water saturation distribution after 113 days of production. 100% saturation is white, 0% saturation is black.



Figure 14: The change in water saturation: 56 days – initial state. +100% is white, –100% is black.



Figure 15: The change in water saturation: 113 days – initial state. +100% is white, –100% is black.



Figure 16: The initial gas saturation distribution. 100% saturation is white, 0% saturation is black.



Figure 17: The gas saturation distribution after 56 days of production. 100% saturation is white, 0% saturation is black.



Figure 18: The gas saturation distribution after 113 days of production. 100% saturation is white, 0% saturation is black.



Figure 19: The change in gas saturation: 56 days – initial state. +100% is white, –100% is black.



Figure 20: The change in gas saturation: 113 days – initial state. +100% is white, –100% is black.

ROCK PHYSICS

Given the fluid-flow simulation data and reservoir geology, we use rock physics analysis to transform pressure, temperature and saturation data into P- and S-wave velocity (V_p , V_s), and density distributions within the reservoir. First, the dry rock properties are estimated from laboratory core sample measurements as a function of mineralogy, porosity, pressure and temperature. Then, effective bulk moduli are computed for three-phase fluid mixtures of oil, gas and water, including the effects of temperature and pressure. Finally, saturated rock properties are calculated using Gassmann's equation to combine the dry-rock data and effective fluid moduli as a function of pressure, temperature, porosity, and fluid saturation.

Dry rock properties

Porosity effect

Our estimates of dry rock properties in the reservoir are based on the results in a similar reservoir reported by Blangy and Strandenes (1991) and Blangy (1992), which involved laboratory experiments conducted on 38 core samples. In the reservoir sand, quartz is the dominant constituent, with volumetric content between 50% and 80%, feldspar content is almost constant at 20%, and mica volumetric content varies between 0% and 25%. Ultrasonic compressional and shear wave velocities were measured at varying differential hydrostatic stress from 5 to 30 MPa. Overburden pressure is approximately 34 MPa and pore pressure varies close to 16 MPa with differential pressure close to 18 MPa. Thus we have chosen to rely on the core lab data set measured at a differential pressure of 20 MPa. Figure ?? shows a scatter plot of the Blangy and Strandenes V_p core measurements made as a function of reservoir sand porosity at 20 MPa differential pressure. Figure ?? shows a similar scatter plot for V_s for varying porosities at 20 MPa differential pressure. We have computed the densities of the core samples based on their reported mineralogy volume fractions. Our dry density values are plotted in Figure ?? at reservoir conditions. Based on the dry V_p , V_s and density data, we calculated the dry bulk moduli K_{dry} and dry shear moduli G_{dry} of the 38 core samples using the relation:

$$K_{dry} = \rho(V_p^2 - \frac{4}{3}V_s^2) \quad ; \quad G_{dry} = \rho V_s^2, \quad (1)$$

where ρ is the dry density. The results of the K_{dry} and G_{dry} calculations are shown in Figures ?? and ?. We did a least-squares linear fit to the data and found:

$$K_{dry} \approx 9357 - 16526\phi \text{ (MPa)}, \quad (2)$$

and

$$G_{dry} \approx 11291 - 22840\phi \text{ (MPa)}, \quad (3)$$

where ϕ is porosity on a scale of 0.0–1.0. The standard deviation of the relative errors for each fit is about 10% for K_{dry} and 5% for G_{dry} . **Pressure effect**

Additionally, we need to know the properties of dry rocks with changing pore pressure. We considered measurements by Han (1986) on unconsolidated Ottawa sand (porosity 33%) that is structurally similar to many North Sea reservoir rocks. Han measured dry V_p and V_s

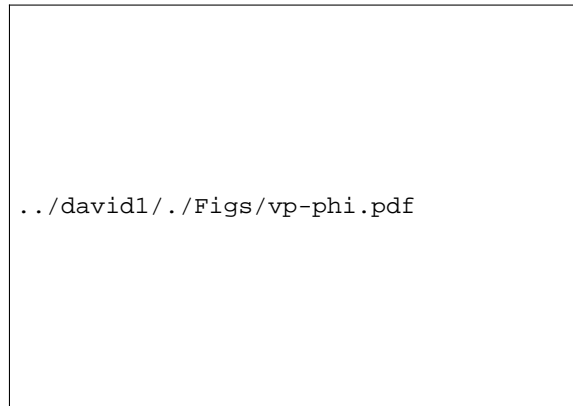


Figure 21: Dry V_p measured versus porosity at 20 MPa differential pressure (after Blangy and Strandenes).

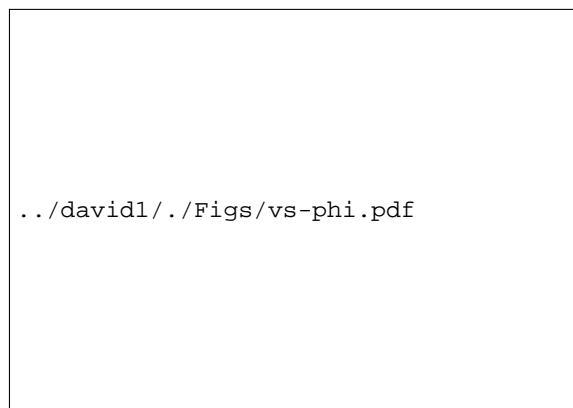


Figure 22: Dry V_s measured versus porosity at 20 MPa differential pressure (after Blangy and Strandenes).

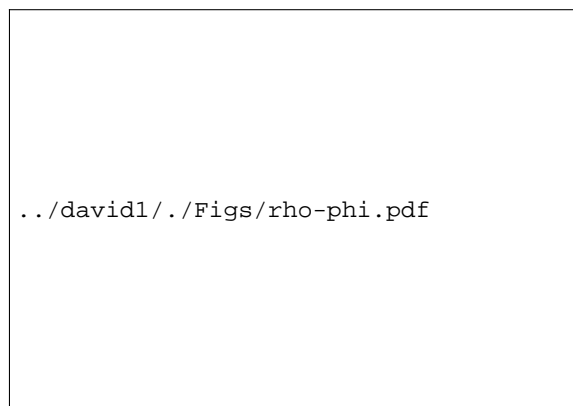


Figure 23: Dry density versus porosity calculated from mineralogy at reservoir conditions.



Figure 24: Dry bulk modulus K_{dry} calculated versus porosity at 20 MPa differential pressure.



Figure 25: Dry shear modulus G_{dry} calculated versus porosity at 20 MPa differential pressure.

as a function of confining hydrostatic stress, which we converted into velocity as a function of pore pressure, as shown in Figure ???. A similar plot shows the variation in velocity with temperature, but we omit this since our reservoir under study does not change temperature during the simulated oil production.

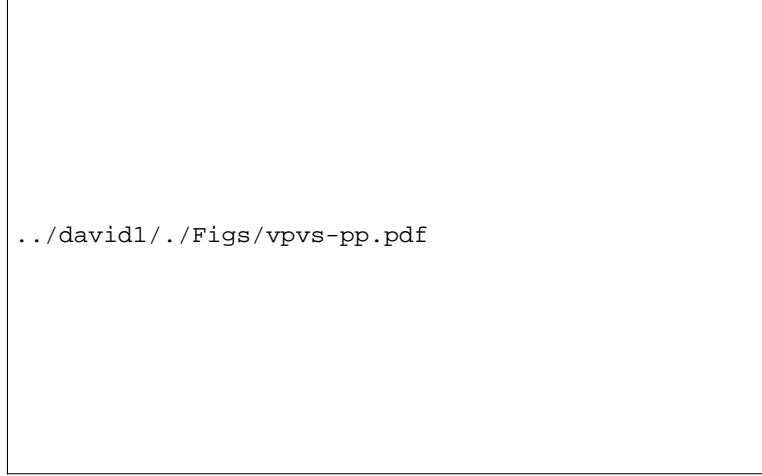


Figure 26: Compressional and shear wave velocities in dry Ottawa sandstone versus pore pressure at 51 MPa overburden pressure (after Han, 1986).

Saturated rock properties

The velocity effect of saturation can be calculated at seismic frequencies by using Gassmann's formulas (e.g., Bourbié et al., 1987). This formula relates the effective elastic moduli of a dry rock to the effective moduli of the same rock containing fluid:

$$\frac{K_{sat}}{K_{solid} - K_{sat}} = \frac{K_{dry}}{K_{solid} - K_{dry}} + \frac{K_{fluid}}{\phi(K_{solid} - K_{fluid})}, \quad (4)$$

and

$$G_{sat} = G_{dry}, \quad (5)$$

where K_{sat} and G_{sat} are the effective bulk and shear moduli of the saturated rock. Gassmann's relations require knowledge of the effective shear and bulk moduli of the dry rock (G_{dry} and K_{dry}), the bulk modulus of the mineral material making up the rock (K_{solid}), the effective bulk modulus of the saturating pore fluid (K_{fluid}), and the porosity ϕ . From Gassmann's formula we derive

$$K_{sat} = K_{solid} \frac{\phi K_{dry} - (1 + \phi) K_{fluid} K_{dry} / K_{solid} + K_{fluid}}{(1 - \phi) K_{fluid} + \phi K_{solid} - K_{fluid} K_{dry} / K_{solid}} \quad (6)$$

and use this last expression to compute the bulk modulus of saturated rock from dry data. For partially saturated rocks at sufficiently low frequencies, we use an effective modulus K_{fluid} for the pore fluid that is an isostress average of the moduli of the liquid and gaseous phases:

$$\frac{1}{K_{fluid}} = \frac{S}{K_{liquid}} + \frac{(1 - S)}{K_{gas}}. \quad (7)$$

This requires knowledge of the bulk modulus of the liquid phase (K_{liquid}), the bulk modulus of the gas phase (K_{gas}), and the saturation values (S). In general, if the pore fluid includes more than two phases, we calculate the mixture's effective bulk modulus K_{fluid} based on the the number of fluid components N , the volumetric concentrations c_i of the i th component, and their bulk moduli K_i :

$$\frac{1}{K_{fluid}} = \sum_{i=1}^N \frac{c_i}{K_i} . \quad (8)$$

Finally, we use the following formulas to find seismic velocities in saturated rocks:

$$V_{psat} = \sqrt{\frac{(K_{sat} + \frac{4}{3}G_{sat})}{\rho_{sat}}} \quad (9)$$

and

$$V_{ssat} = \sqrt{\frac{G_{sat}}{\rho_{sat}}} , \quad (10)$$

where ρ_{sat} is the density of the saturated rock:

$$\rho_{sat} = (1 - \phi)\rho_{solid} + \phi\rho_{fluid} , \quad (11)$$

ρ_{solid} is the density of the solid phase, and ρ_{fluid} is the density of the fluid mixture obtained as an arithmetic mean of the volume-concentration-weighted fluid density components ρ_i :

$$\rho_{fluid} = \sum_{i=1}^N c_i \rho_i . \quad (12)$$

We assume the following typical values for the reservoir water: a density of 1.0 g/cc and a bulk modulus of 2250 MPa. This process allows us to calculate fluid properties that depend on fluid-flow saturation values. These properties will depend on pressure and temperature because the bulk modulus and density of the reservoir gas are affected by these two parameters. As an example, we convert the pressure-dependent Ottawa sand compressional velocity of Figure ?? to be dependent on both pressure and fluid saturation (oil, water or gas), as shown in Figure ??.

Pressure-dependent gas properties

We calculate pressure- and temperature-dependent gas properties as in Batzle and Wang (1992), and assume that the reservoir gas is primarily methane with a specific gravity 0.55. Pseudo-reduced pressure and temperature are related to reservoir pore pressure and temperature as:

$$P_{pr} = \frac{P}{(4.892 - 0.4048 G)} , \quad (13)$$

and

$$T_{pr} = \frac{T_a}{(94.72 + 170.75 G)} , \quad (14)$$

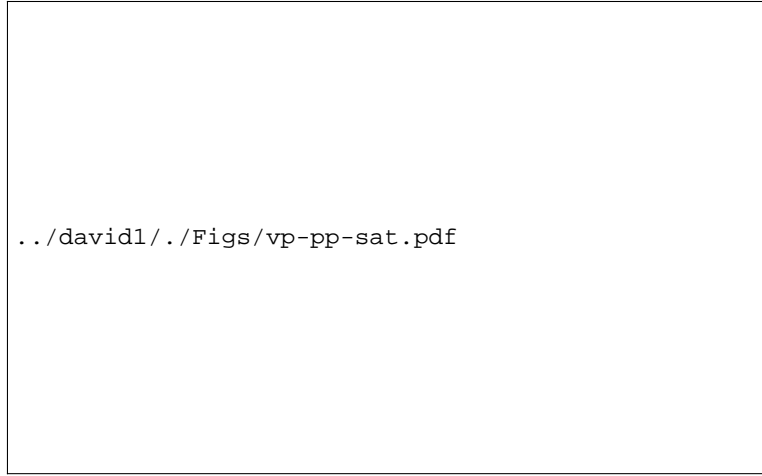


Figure 27: Compressional velocity in Ottawa sand as a function of pore pressure and (oil,water,gas) saturation.

where G is the gas specific gravity, T_a is absolute temperature: $T_a = \text{°C} + 273$. The pressure is given in MPa. Gas density is

$$\rho_{gas} \approx \frac{28.8 GP}{ZRT_a}, \quad (15)$$

where the “Z-factor” is defined as:

$$Z = [0.03 + 0.00527(3.5 - T_{pr})^3] P_{pr} + (0.642 T_{pr} - 0.007 T_{pr}^4 - 0.52) + E, \quad (16)$$

and

$$E = 0.109(3.85 - T_{pr})^2 e^{-\alpha}, \quad (17)$$

$$\alpha = [0.45 + 8(0.56 - T_{pr}^{-1})^2] P_{pr}^{1.2} T_{pr}^{-1} \quad (18)$$

and $R = 8.31$ is the universal gas constant. The adiabatic gas bulk modulus K_s is:

$$K_s \approx \frac{P\gamma_0}{\left(1 - \frac{P_{pr}}{Z} \frac{\partial Z}{\partial P_{pr}}\right)_T} \quad (19)$$

where

$$\gamma_0 = 0.85 + \frac{5.6}{P_{pr} + 2} + \frac{27.1}{(P_{pr} + 3.5)^2} - 8.7 e^{-0.65(P_{pr}+1)}, \quad (20)$$

and $(\partial Z/\partial P_{pr})$ can be calculated from Equation 16 for Z . This rock physics analysis allows us to calculate seismic velocities in saturated reservoir rock as a function of mineralogy, fluid type and saturation value, pore pressure and temperature. Therefore, we can map P-wave and S-wave velocity and density as a function of the reservoir grid directly from the fluid-flow simulation values of pressure, temperature, and oil, gas and water saturation.

P-wave velocity

Figure ?? shows the initial V_p velocity distribution, which is largely controlled by the porosity at this state. Velocities range from 2.1 km/s (dark gray) to 3.3 km/s (white). Figures ?? and ?? show the V_p distribution after 56 and 113 days of oil production. A V_p decrease from about 2.5 to 2.1 km/s is evident in the area that the gascap is expanding downward, which is due largely to gas replacing oil in the pore space. Figures ?? and ?? show the changes in V_p after 56 and 113 days of production. There is a -400 m/s decrease in V_p in the gas cone, and a smaller $+100$ m/s increase in V_p where the aquifer has coned upward from below allowing water to displace oil. Density variations in the reservoir are of the same polarity as the V_p variations. Density decreases from about 2.1 g/cc to 1.8 g/cc in the gas cone, and increases to about 2.15 g/cc in the water cone. Because these plots look qualitatively similar to the V_p plots, they have been omitted here for brevity.



Figure 28: The initial V_p distribution. Velocities range from 2.1 km/s (dark gray) to 3.3 km/s (white).

S-wave velocity

Figure ?? shows the initial V_s velocity distribution, which is mostly due to porosity variations. Velocities range from 1.2 km/s (dark gray) to 2.0 km/s (white). Figures ?? and ?? show the V_s distribution after 56 and 113 days of oil production. A V_s increase from about 1.5 to 1.6 km/s is evident in the area that the gascap is expanding downward, which is due to the density decrease of gas replacing oil in the pore space. Since the pore pressure change is too small to affect G_{dry} much, and fluid saturation does not affect the shear modulus at all according to Gassmann's equations 5, the decrease in density due to gas replacing oil must therefore



Figure 29: The V_p distribution after 56 days of production. Velocities range from 2.1 km/s (dark gray) to 3.3 km/s (white).



Figure 30: The V_p distribution after 56 days of production. Velocities range from 2.1 km/s (dark gray) to 3.3 km/s (white).



Figure 31: The change in Vp: 56 days – initial state. +140 m/s is white, –400 m/s is black.



Figure 32: The change in Vp: 113 days – initial state. +140 m/s is white, –400 m/s is black.

increase V_s . Figures ?? and ?? show the changes in V_s after 56 and 113 days of production. There is a +80 m/s increase in V_s in the gas cone, and a smaller -20 m/s decrease in V_s where the aquifer has coned upward from below allowing water to displace oil.



Figure 33: The initial V_s distribution. Velocities range from 1.2 km/s (dark gray) to 2.0 km/s (white).

SEISMIC MONITORING ANALYSIS

This section of the paper deals with the seismic monitoring analysis of the North Sea reservoir in simulated production. In particular, we discuss the global seismic model construction, and upscaling of fine-scale reservoir properties to an equivalent seismic-scale reservoir model for seismogram calculation. We used a Kirchhoff reflectivity method to simulate a prestack surface seismic survey at each of three separate monitoring phases of production. These three prestack datasets were then processed in a conventional manner to produce stacked and prestack-migrated reflectivity images. Difference images obtained by subtracting combinations of stacked and migrated sections clearly show that reservoir fluid production is visible in the seismic data and can be monitored in the presence of reasonable levels of seismic noise.

North Sea seismic model

A global seismic model of P- and S-wave velocity and density was constructed based on information provided by Norsk Hydro, as shown in Figure ?. The global model consists of a 1-D “overburden” macro-model merged with a 2-D fine-scale reservoir model. A vertically-stratified “overburden” model was designed to optimize intensive synthetic seismogram com-



Figure 34: The Vs distribution after 56 days of production. Velocities range from 1.2 km/s (dark gray) to 2.0 km/s (white).



Figure 35: The Vs distribution after 56 days of production. Velocities range from 1.2 km/s (dark gray) to 2.0 km/s (white).



Figure 36: The change in V_s : 56 days – initial state. +80 m/s is white, –20 m/s is black.



Figure 37: The change in V_s : 113 days – initial state. +80 m/s is white, –20 m/s is black.

putation while still preserving the overall character of the stacked section and the simple $v(z)$ interval velocity model provided by Norsk Hydro. The macro-layers of the overburden model were chosen to approximate the position and relative reflection amplitude of reflectors seen in the Norsk Hydro stacked section at the well location, which penetrates the reservoir horizontally at about 1.55 km depth at the 1.5–2.0 km midpoint distance in the coordinate system shown in Figure ???. Three curves of V_p , V_s and density are shown at the well location as a



Figure 38: P-wave velocity model consisting of a 1-D “overburden” structure and a 2-D fine-layered reservoir zone at 1.5–1.6 km depth.

function of depth in Figure ???. The 1-D overburden increases slowly with depth down to the top of the reservoir, with a slight low velocity zone in the middle depth section. The reservoir zone at 1.55 km depth has a strong low velocity and density contrast due to the gas cap, and then increases to a regional profile at and below the base of the reservoir.

Upscaled reservoir model

Figure ?? shows a fine-layered model of P-impedance calculated from the fluid-flow simulations provided by Norsk Hydro. The fine-scale seismic properties were mapped from reservoir pressure, temperature, relative saturation values of oil, water and gas, and porosity as described by the previous rock physics section of this report. An issue of upscaling arises because in situ reservoir properties measured at very small spatial scales are not necessarily the same properties that a seismic wavefield samples at larger seismic wavelength scales. The reservoir simulation used a grid mesh that represented fine-layering on a scale as small as 1 meter in thickness. It would be computationally prohibitive to compute prestack seismograms on a mesh that small, and may not be numerically justifiable even if one could do so. Instead, we consider an “equivalent medium” sampled on a coarse mesh that propagates seismic wave-



Figure 39: Initial velocity and density model at the surface well position (2 km).



Figure 40: P-impedance reservoir model evaluated on a fine grid mesh.

fields which are dynamically equivalent to the waves that would have propagated in the true fine-layered medium. This equivalent medium can be approximated by a spatially weighted average of elastic compliance and density which attempts to conserve the stress-strain energy of elastic waves and the mass of the medium (Schoenberg and Muir, 1989; Muir et al., 1992). Figure ?? shows the upscaled coarse-mesh equivalent reservoir model of P-impedance. Similar upscaled equivalent models were calculated for S-impedance and density. Figure ?? shows the fine-scale and upscaled V_p , V_s and density curves in the reservoir at the wellbore location. The upscaling was done as follows. First, an over-sampled representation of the fine scale reservoir model was obtained at a sampling interval of 0.5 m in depth and 2.5 m in midpoint distance. Next, the equivalent medium averaging was done for isotropic elastic compliance and density onto a coarse mesh of 5 m by 5 m in depth and midpoint. The upscaled compliances were then converted to P- and S-impedance to give the final upscaled seismic models at a mesh interval that is about one tenth of a seismic wavelength, as opposed to the original 1/100th of a seismic wavelength.



Figure 41: Upscaled P-impedance reservoir model on a coarse grid mesh. Obtained by averaging elastic compliance and density from fine to coarse mesh scales.

Time-variant seismic models

Using the equivalent medium upscaling procedure described above, P- and S-impedance, and density models were computed for each of the three production monitoring phases. The monitors simulate fluid flow in the reservoir due to production in a horizontal well after one day, 56 days, and 113 days of production. For simplicity, we name the day-one simulation as the “base survey”, and the subsequent 56 and 113 day monitors as “monitor 1” and “monitor 2” respectively. **P-impedance**



Figure 42: Reservoir velocity and density model curves. Blocky curves are fine-mesh values at 0.5 m depth intervals, smooth curves are equivalent upscaled values at 5 m intervals.

Figure ?? shows the initial state of seismic P-impedance (I_p). Figures ?? and ?? show the I_p distributions after 56 and 113 days of oil production. In the vicinity of the wellbore, an asymmetric decrease in P-impedance is evident during production. This decrease in P-impedance is more clearly shown at 2 km in the curves of Figure ?. The decrease in P-impedance is due to downward coning and enlargement of the gas cap near the wellbore during production of the thin oil zone, and the asymmetry is probably due to lateral change in perforation density along the horizontal well. During the total production time, the P-impedance decreases in the reservoir by a maximum relative contrast of about 15%, and is spread over a zone that is approximately 500 m wide and 15 m thick. This change in P-impedance will be shown later to cause a significant seismic reflection response. **S-impedance**

Figure ?? shows the initial state of seismic S-impedance (I_s). Figures ?? and ?? show the I_s distributions after 56 and 113 days of oil production. Barely any change in S-impedance is visible in the zone of gas coning. This is because the shear modulus is not sensitive to fluid-saturation changes, and the pressure effect is also negligible at these small drawdown pore pressure changes. V_s has slightly increased due to a small decrease in density, and these two effects tend to cancel each other for S-impedance, which is the product of V_s and density. Thus, the overall result is a slight decrease in shear impedance during oil-replacement by expanding gas during production. The S-impedance curves of Figure ?? at the well location show that the S-impedance decreases a maximum of 5% at the cone, but is more representatively a decrease of about 2% spread over the entire zone of gas coning.



Figure 43: Initial P-impedance distribution in enlarged reservoir zone. I_p ranges from 3.8 (dark gray) to 7.8 km/s-g/cc (white).



Figure 44: P-impedance distribution after 56 days of oil production. The averaged I_p values have decreased by about 10% in the production interval.



Figure 45: P-impedance distribution after 113 days of oil production. The averaged I_p values have decreased by about 15% in the production interval.



Figure 46: Reservoir time-varying P-impedance curves. Averaged P-impedance decreases significantly by about 10–15% with increasing production time due to gas coning.



Figure 47: Initial S-impedance distribution in enlarged reservoir zone. I_s ranges from 2.5 (dark gray) to 4.2 km/s-g/cc (white).



Figure 48: S-impedance distribution after 56 days of oil production. The averaged I_s values have decreased by about 3% in the production interval.



Figure 49: S-impedance distribution after 113 days of oil production. The averaged I_s values have decreased by about 5% in the production interval.



Figure 50: Reservoir time-varying S-impedance curves. S-impedance decreases slightly by about 2–5% with increasing production time due to gas coning.

Kirchhoff seismogram modeling

Given the reservoir models during each of the three phases of oil production, synthetic surface reflection seismic data can be generated for each time snapshot of production. The synthetic seismograms are calculated based on the generalized Kirchhoff body force scattering theory of Lumley and Beydoun (1993). This theory combines Zoeppritz plane-wave reflection and Rayleigh-Sommerfeld elastic diffraction responses. The modeling theory can generate the correct AVO response for locally planar reflectors, and merge into diffraction where elastic properties vary spatially faster than a seismic wavelength. However, since the Green's tensors are WKBJ ray-valid, only primary reflections and diffractions are computed. Higher order multiple scattering or phenomena such as surface waves are not modeled. The modeling theory is based on a volume integration of the body force equivalent of the $\hat{P}\hat{P}$ coefficient:

$$\hat{\mathbf{a}}_r \cdot \mathbf{u}^P(\mathbf{x}_r) = \int_{\mathcal{V}} ik A_s A_r e^{i\omega\tau_{sr}} \hat{P}\hat{P} \cos\phi_r d\mathcal{V}. \quad (21)$$

\mathbf{u}^P is the P-P scattered vector wavefield measured at the receiver position \mathbf{x}_r , and projected onto an arbitrary receiver component direction $\hat{\mathbf{a}}_r$. A_s and A_r are the elastic WKBJ Green's function amplitudes from the source and receiver positions respectively, to each subsurface scattering point \mathbf{x} in the volume \mathcal{V} . Similarly, $\tau_{sr} = \tau_s + \tau_r$ is the total traveltime from source to scatterer to receiver. The factor $\cos\phi_r$ is the non-geometric diffraction angle as shown in Figure ??, and is unity along the Snell reflection path (specular), and variable otherwise. The $\hat{P}\hat{P}$ factor is the plane-wave Zoeppritz elastic P-P reflection coefficient, and k is the spatial wavenumber $k = \omega/\alpha$. The incident arrival direction vector $\hat{\mathbf{t}}^P$ is drawn in Figure ?. The volume integration gives the impulse response seismograms which can then be filtered to any desired bandwidth and convolved with a wavelet. Additionally, spatially-uncorrelated Gaussian distributed noise, filtered to match the same frequency bandwidth as the seismic signal, may also be added to produce fairly realistic primary reflection data with accurate AVO responses and the presence of seismic noise.



Figure 51: Generalized Kirchhoff reflection and diffraction angle geometries.

CMP gather analysis

Synthetic seismograms were generated at the CMP location directly above maximum coning, at 2 km distance in the midpoint coordinate. A typical marine acquisition geometry of 60-fold CMP gathers was used with a near offset of 250 m and a 3 km cable length. The bandwidth of the seismic data have corner frequencies of 5, 10, 60 and 80 Hz. Random spatially-uncorrelated Gaussian noise was filtered to the same bandwidth and added to make the “noisy” seismic traces. The signal-to-noise (S/N) amplitude ratio is about 3:1 at the main reservoir reflections at 1.6 seconds. For display purposes, the CMP gathers have been divergence-corrected and compensated for source-receiver amplitude directivity. Figure ?? shows a close-up of the reservoir reflections in the noise-free CMP gather at the time of the base survey. Figure ?? shows the same CMP gather but with added noise. The top of the reservoir is the first negative reflection at about 1.55 seconds, and the complex wavetrain following is due to the fine-layered nature of the reservoir zone. Since the velocity increases dramatically from the top to the bottom of the reservoir, the reservoir reflections tend to coalesce into one single low-frequency high-amplitude waveform at far offsets. The reservoir reflections are still prominent in the noisy CMP gather, although the shallower arrivals at far offsets are not.

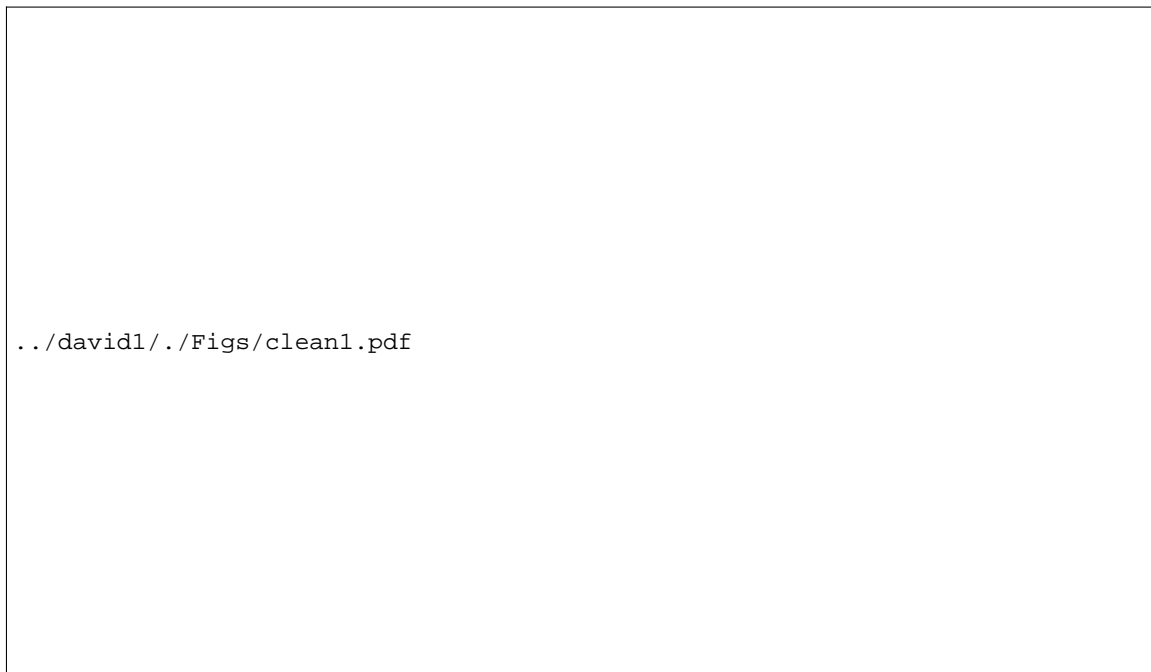


Figure 52: Noise-free CMP gather at the well location: base survey.

Figures ?? and ?? show the same CMP gathers at the time of monitor 1. Due to the decrease in P-impedance, the negative reflection at 1.6 seconds, slightly below the top of the reservoir, has increased in magnitude, as has its positive side-lobe at about 1.61 seconds. There is also an apparent increase in wavetrain amplitude with offset, compared to the base survey CMP gathers. Both the increased near-offset reflection amplitude and the AVO enhancement are visible in the noisy CMP gathers. Figures ?? and ?? show the same CMP gathers at the time of monitor 2. Again, due to the decrease in P-impedance, there is an increase in near-offset



Figure 53: Noisy CMP gather at the well location: base survey.



Figure 54: Noise-free CMP gather at the well location: first monitor survey.



Figure 55: Noisy CMP gather at the well location: first monitor survey.

amplitude and AVO, although not perceptibly different than monitor 1 from this view in the CMP gathers. Figures ?? and ?? show the “difference gathers” obtained by subtracting the CMP gathers of the base survey from those of monitor 1. A single Hilbert-shaped diffraction waveform expresses the difference between the two surveys. The dipole Hilbert shape arises from a negative P-impedance contrast at the top of the coning zone, followed closely by an increase in P-impedance in the unchanged reservoir at the base of the cone. The difference diffraction is visible in the noisy data with a S/N ratio of about 1.5:1. Figures ?? and ?? show the difference gathers obtained by subtracting the CMP gathers of the base survey from those of monitor 2. A stronger dipole diffraction waveform expresses the difference between the two surveys, which is clearly visible in the noisy data with a S/N ratio of about 2:1.

Stacked section analysis

Three prestack marine surveys were simulated to monitor the oil production in the North Sea reservoir. Each survey consisted of 161 60-fold CMP gathers with noise, as described in the previous section. The midpoint spacing was 25 m such that the 161 CMP gathers in each survey covered a total line length of 4 km. Each gather had a minimum source-receiver offset of 250 m and a maximum offset of 3.250 km, and a total record length of 2.4 seconds at a 4 ms sample interval. The prestack data were muted at water velocity, divergence corrected, and amplitude corrected for source and receiver directivity prior to stacking. No wavelet deconvolution was applied. A 1-D rms stacking velocity was computed from the 1-D overburden interval velocity model, without the detailed 2-D reservoir zone velocity variations, and was



Figure 56: Noise-free CMP gather at the well location: second monitor survey.



Figure 57: Noisy CMP gather at the well location: second monitor survey.

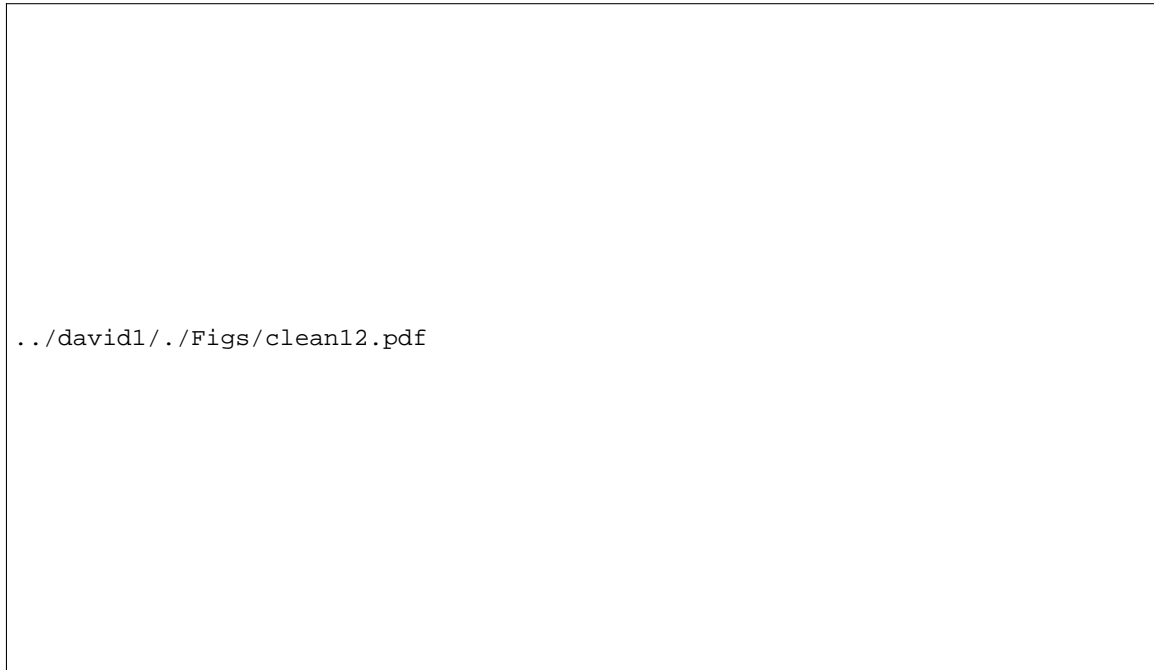


Figure 58: Difference gather obtained by subtracting the noise-free base survey gather from the first monitor gather.

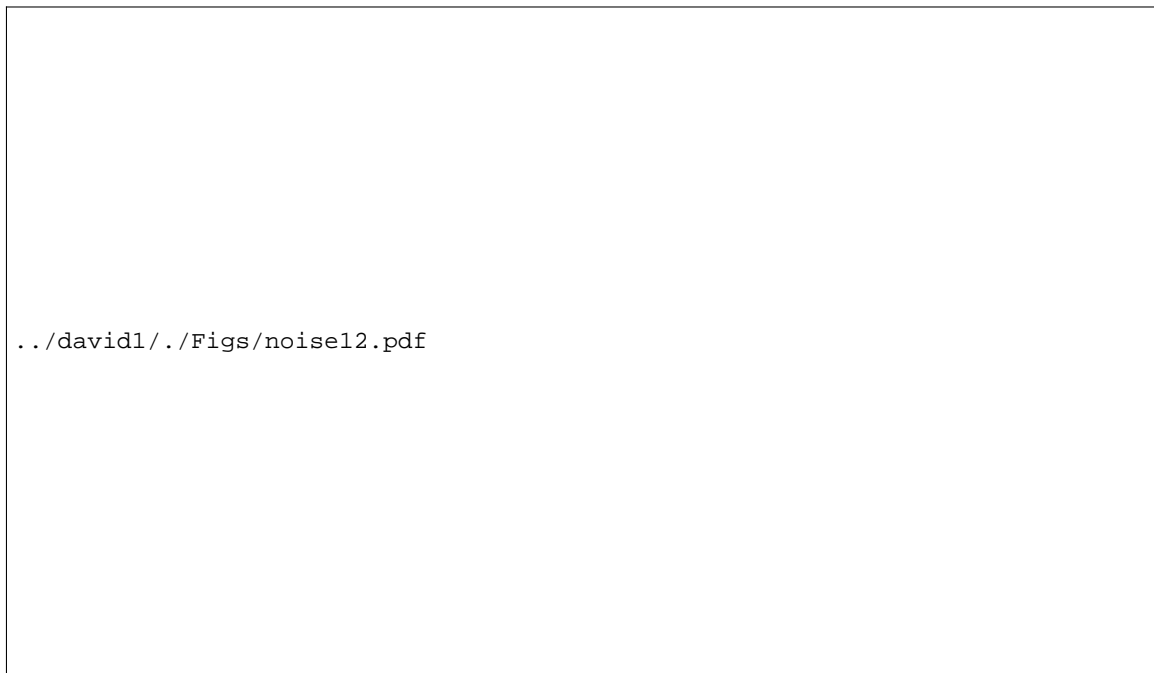


Figure 59: Difference gather obtained by subtracting the noisy base survey gather from the first monitor gather.

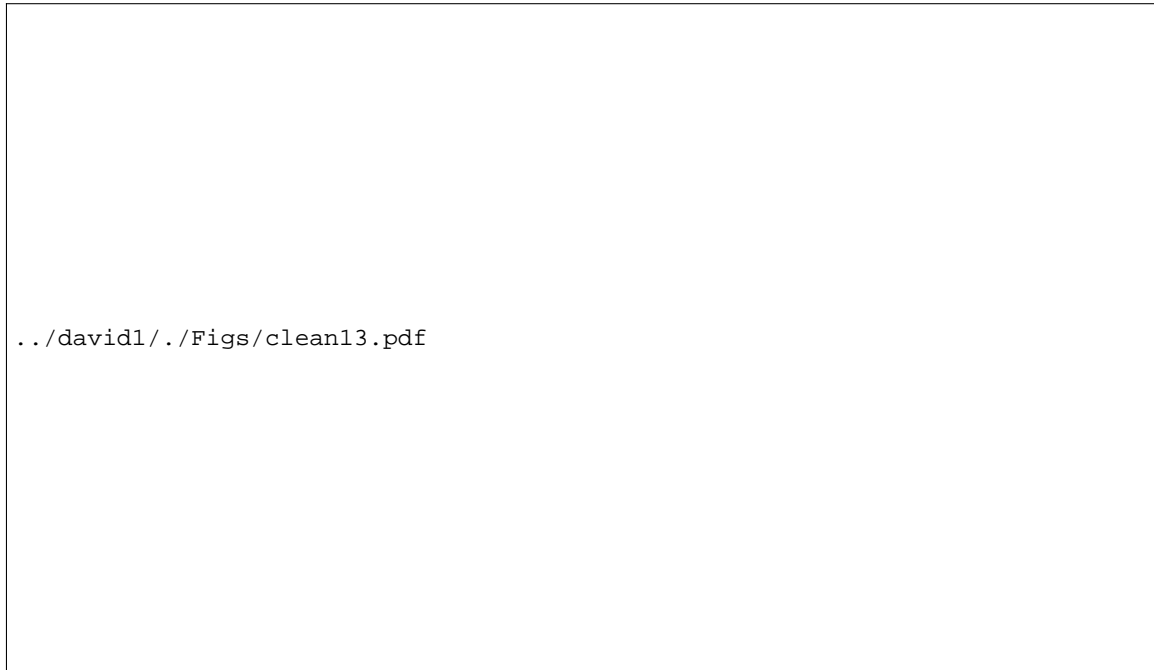


Figure 60: Difference gather obtained by subtracting the noise-free base survey gather from the second monitor gather.

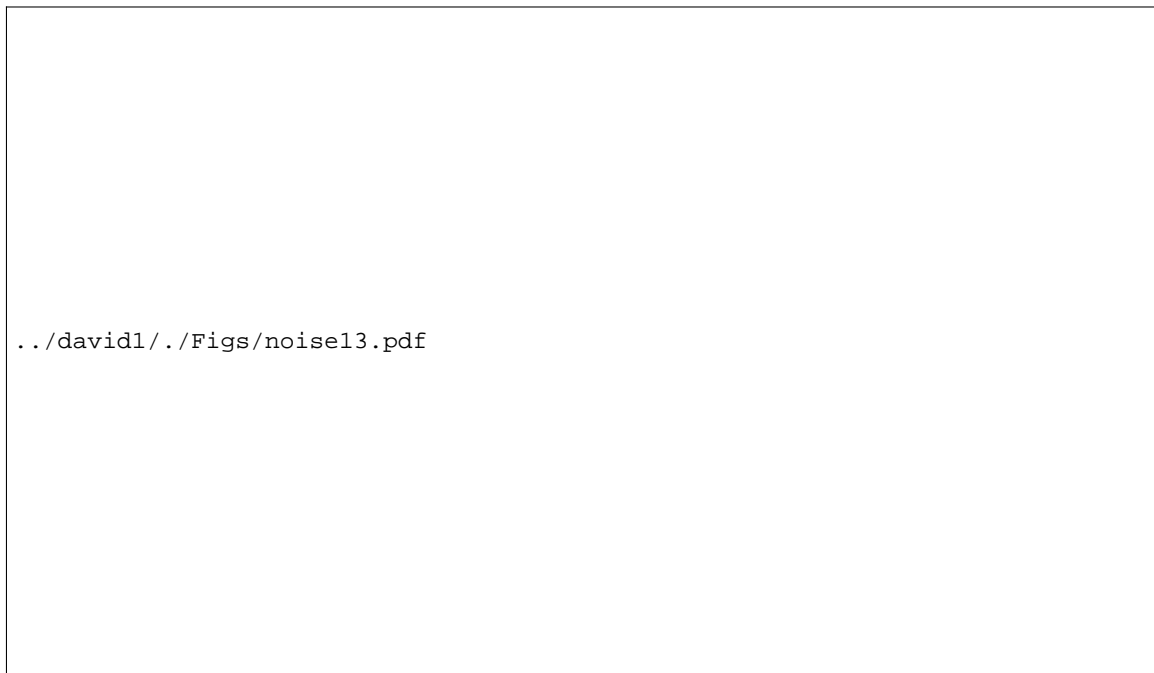


Figure 61: Difference gather obtained by subtracting the noisy base survey gather from the second monitor gather.

used to perform the anti-aliased NMO stack. This emulates a standard processing sequence in which only macro velocity information is known prior to stacking and migration. Figure ?? shows the complete stacked section from the base survey, which is a fairly good but idealized approximation to the real stacked paper section provided by Norsk Hydro. Figure ?? shows a close-up of the reservoir in the base survey stacked section. Figures ?? and ?? show the same reservoir close-up of the monitor 1 and 2 stacked sections respectively. Subtle changes in the form of increased bright amplitudes in the stacked section are evident in the vicinity of the wellbore and gas coning at 2 km and 1.6 s. Also, some diffraction tails are present due to the point-source-like, strong impedance contrast at the lower tip of the gas cone, and are especially evident in the monitor 2 stack. Figure ?? shows the difference section obtained by

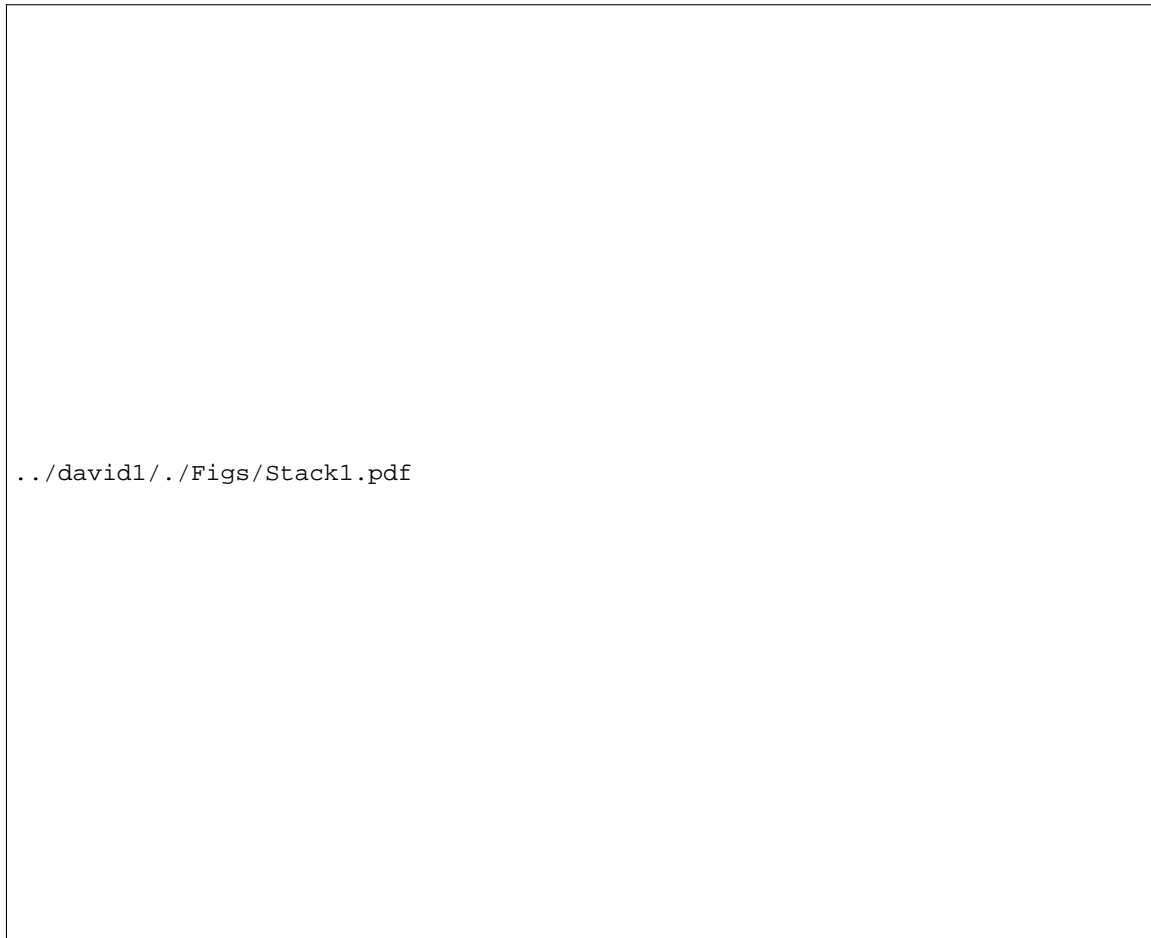


Figure 62: Base survey stacked section.

a simple subtraction of the base survey stack from the monitor 1 stack. The gas coning clearly stands out from the background seismic noise as a bright spot at 2 km and 1.6 s. A small diffraction tail is present at the tip of the gas cone. There are also some low amplitude seismic differences at the lateral edges of the reservoir. These seismic difference amplitudes are due directly to pressure and saturation changes calculated in the fluid-flow simulation, and are not seismic modeling or processing artifacts. These boundary pressure and saturation changes may be low-amplitude fluid-flow simulation artifacts caused by a sparse simulation mesh or



Figure 63: Base survey stacked section.



Figure 64: Monitor 1 stacked section. Note the bright amplitudes due to gas coning.



Figure 65: Monitor 2 stacked section. Note the development of diffractions “d” from the gas cone.

imperfect boundary conditions in the fluid-flow modeling algorithm, since they are visible in the simulation data. Figure ?? shows the stacked difference section comparing monitor 2 to the base survey. The amplitude of the main bright spot and its diffraction tails has increased considerably, and is clearly identifiable from the background noise. At the same plotting scale, Figure ?? shows the stacked difference section comparing the seismic change between monitor 2 and monitor 1. The main gas cone anomaly is quite weak, which indicates that the major seismic response to oil production occurs between monitor 1 and the base survey. Monitor 2 adds extra information on the lateral extent, depth, and thickness of the gas cone, but the major “detection” of reservoir change occurs by the time of monitor 1 (56 days into production).

Prestack migration analysis

The same three prestack datasets described in the previous section were analyzed after prestack migration. Preprocessing included a simple water-velocity mute. No geometrical-spreading correction or source-receiver amplitude directivity were compensated for in the preprocessing phase, since the prestack migration code incorporates these corrections in a more physical manner. A true-amplitude Kirchhoff prestack migration code was used that includes operator anti-aliasing (Lumley, 1993; Lumley and Claerbout, 1993). Figure ?? shows the complete prestacked-migrated section from the base seismic survey. Figure ?? shows a close-up of the reservoir zone in the base survey migrated section. In comparison with the base stack of Figure ??, one can see the improvement in S/N ratio and spatial resolution of the reservoir boundaries and internal reflections that prestack migration brings. Figures ?? and ?? show the

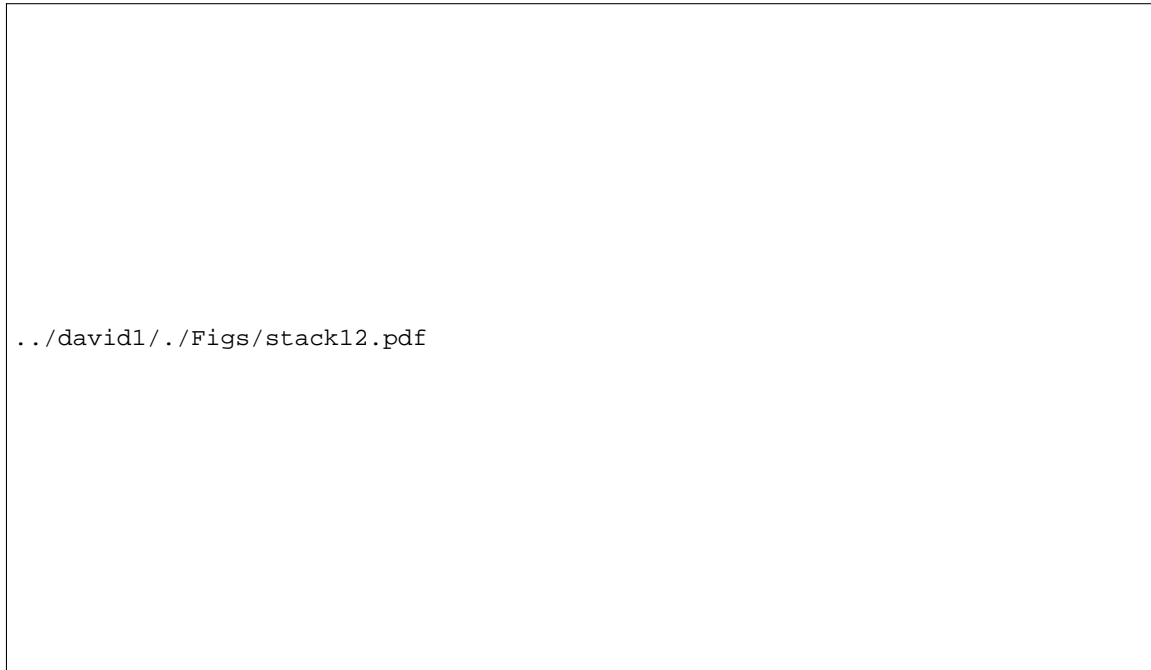


Figure 66: Base survey stacked section subtracted from the first monitor stacked section. Note the bright amplitudes due to gas coning.

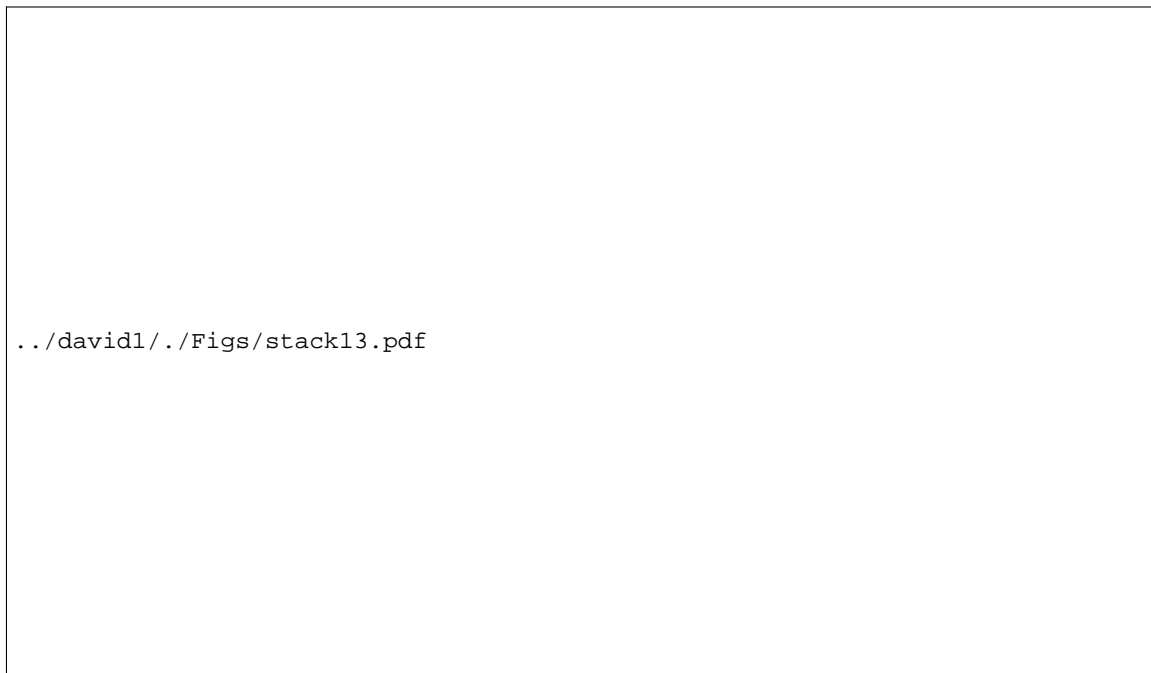


Figure 67: Base survey stacked section subtracted from the second monitor stacked section. Note the increased bright amplitudes and diffractions due to gas coning.



Figure 68: First monitor stacked section subtracted from the second monitor stacked section. Note the weak amplitudes due to gas cone movement between monitor surveys.

prestack migrated reservoir sections from the monitor 1 and monitor 2 surveys respectively. There is a well-defined increase in bright-spot amplitude at the position of the gas cone, and its spatial resolution is very good compared to the original time-variant impedance models. The migrated sections are not cluttered with diffraction noise as was the case with the stacked sections, and the resolution of the gas cone anomaly is much higher than the blurred stacked section response. This is because stacked seismic data have a resolution on the range of about 1/4 of a Fresnel zone (typically hundreds of meters), whereas prestack migrated images have a resolution on the order of 1/4 of a seismic wavelength (typically tens of meters). Figure ?? shows the difference section obtained by a simple subtraction of the base survey migration from the monitor 1 migration. The gas coning clearly stands out from the background seismic noise as a bright spot at 2 km and 1.6 s, and accurately defines the spatial extent of the true impedance model anomaly. Figure ?? shows the difference section comparison between the monitor 2 and base survey migrations. Again, the seismic response to the gas coning is very clear and accurate in spatial location. Figure ?? shows the change in migrated seismic response between the first and second monitor surveys. As with the stacked section analysis, most of the major detectable seismic response occurs by the time of the first monitor survey, and the difference between the first and second monitors is a more subtle expression of the increase in spatial extent and impedance anomaly of the expanding gas cone.

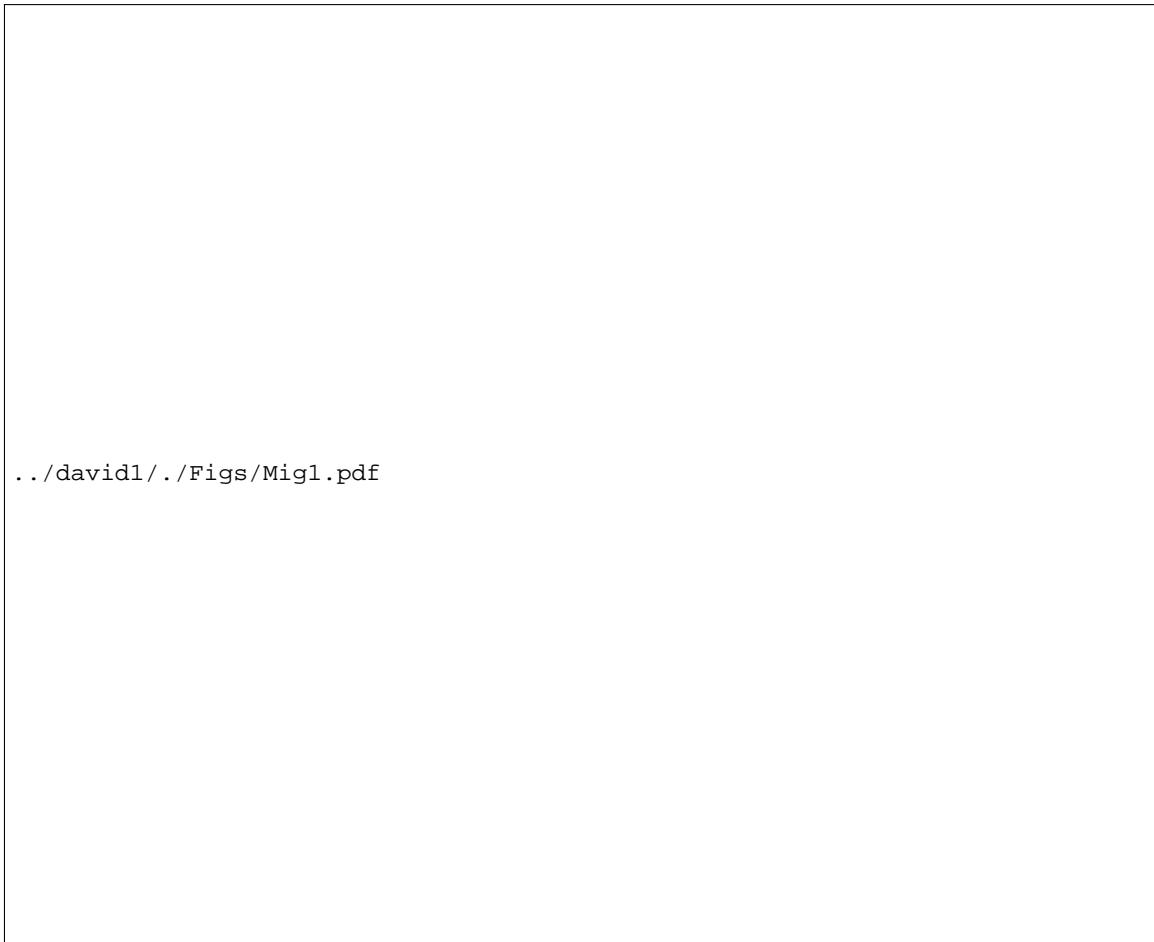


Figure 69: Base survey migrated section.



Figure 70: Base survey migrated section.



Figure 71: Monitor 1 migrated section. Note the bright amplitudes due to gas coning.



Figure 72: Monitor 2 migrated section. Note the increased bright amplitudes due to gas coning.



Figure 73: Base survey migrated section subtracted from the first monitor migrated section. Note the bright amplitudes due to gas coning.



Figure 74: Base survey migrated section subtracted from the second monitor migrated section. Note the increased bright amplitudes due to gas coning.



Figure 75: First monitor migrated section subtracted from the second monitor migrated section. Note the weak amplitudes due to gas cone movement between monitor surveys.

Seismic conclusions

This section of the paper discussed the feasibility of performing a seismic monitoring analysis of the North Sea reservoir in simulated oil production, based on prior fluid-flow simulation and rock physics results. To test seismic monitoring feasibility, detailed reservoir models of elastic impedance and density were constructed that honored the fluid-flow pressure and saturation data, combined with rock physics data and petrophysical relationships. Prestack synthetic seismic surveys were then generated for each of the three production phases: base survey (no production), monitor 1 (56 days of production), and monitor 2 (113 days of production). Using realistic marine seismic recording geometry parameters and noise levels, we were able to successfully detect and monitor dynamic gas-cone movement in the reservoir from seismic monitor data during the fluid-flow simulation of oil production. Evidence of gas-cone evolution is clearly visible in both the stacked and prestack-migrated seismic difference sections at realistic seismic noise levels and seismic frequency bandwidth. In particular, the prestack migrated sections have enough spatial resolution to accurately locate the lateral extent, depth and thickness of the developing gas cone. If a simple detection of reservoir change is the first order goal, then this could be reasonably achieved after only 56 days of production by comparing the base seismic survey stacked section to the first monitor survey stacked section using the differencing technique. If, however, a clear image of the dynamic gas-cone evolution is desired, repeated seismic monitoring of oil production is needed to increase the S/N ratio of the seismic gas-cone response, and robust prestack-migration imaging is required to optimally estimate the spatial extent and amplitude of the evolving gas-cone impedance anomaly.

CONCLUSIONS

We conducted a feasibility study concerned with the likelihood of seismically detecting and monitoring the fluid-flow changes in a North Sea reservoir during solution-gas-drive oil production from a horizontal well. We conducted this hydrocarbon recovery monitoring analysis by: (1) using flow simulation results (pore pressure, and oil, gas and water saturations) and information about the relevant rock properties (dry elastic constants); (2) using rock physics to compute compressional and shear wave impedances in the reservoir from the flow simulation results; (3) conducting elastic modeling to simulate seismic surveys of the recovery process; and (4) mapping the differences between seismic responses at production intervals of 56 and 113 days, and the base seismic survey. Using realistic marine seismic recording geometry parameters and noise levels, we were able to successfully detect and monitor dynamic gascap coning and expansion in the reservoir from seismic monitor data during the fluid-flow simulation of oil production. Feasibility studies such as this may help reduce the financial risk associated with designing and implementing a seismic monitoring project given a pre-monitor engineering and petrophysical reservoir database.

ACKNOWLEDGMENTS

We thank Norsk Hydro for providing us with the reservoir information and fluid-flow simulation data in order to undertake this project. This work was supported by Norsk Hydro and the Sponsors of the Stanford Exploration Project. We thank Francis Muir, Gary Mavko and Tapan Mukerji for useful discussions and assistance related to this study.

REFERENCES

- Blangy, J. P., 1992, Integrated seismic lithologic interpretation: the petrophysical basis, Ph.D. Thesis, Stanford University.
- Blangy, J. P., and Strandenes, S., 1991, Stanford Rock Physics Lab Report, **47**, Stanford University.
- Bourbié, T., Coussy, O., and Zinszner, B., 1987, Acoustics of porous media: Institut Francais du Petrole Publications.
- Eastwood, J., Lebel, P., Dilay, A., and Blakeslee, S., 1994, Seismic monitoring of steam-based recovery of bitumen: *The Leading Edge*, **13**, 242–251.
- Graebner, R., 1993, Geophysics: The potential and limits for reservoir description and monitoring: presented at the 1993 Annual Summer Research Workshop, Soc. Expl. Geophys.
- Greaves, R. J., and Fulp, T. J., 1987, Three-dimensional seismic monitoring of an enhanced oil recovery process: *Geophysics*, **52**, 1175–1187.
- Han, D., 1986, Effects of porosity and clay content on acoustic properties of sandstones and unconsolidated sediments: Ph.D. Thesis, Stanford University.
- Lumley, D. E., 1993, Kirchhoff prestack impedance inversion: a gas reservoir pilot study: Stanford Exploration Project Report, **77**, Stanford University, 211–230.
- Lumley, D. E., and Beydoun, W. B., 1993, Angle-dependent reflectivity estimation by Kirchhoff migration/inversion: Stanford Exploration Project Report, **79**, Stanford University, 205–226.
- Lumley, D. E., and Claerbout, J. F., 1993, Anti-aliased Kirchhoff 3-D migration: a salt intrusion example: Annual SEG Summer Research Workshop on 3-D Seismology, Soc. Expl. Geophys., Expanded Abstracts, 115–123.

Muir, F., Dellinger, J., Etgen, J., and Nichols, D., 1992, Modeling elastic fields across irregular boundaries: *Geophysics*, **57**, 1189–1193.

Nur, A., 1989, Four-dimensional seismology and (true) direct detection of hydrocarbons: the petrophysical basis: *The Leading Edge*, **9**, 30–36.

Pullin, N. E., Jackson, R. K., Matthews, L. W., Thorburn, R. F., Hirsche, W. K., and den Boer, L. D., 1987, 3-D seismic imaging of heat zones at an Athabasca tar sands thermal pilot: 57th Annual Internat. Mtg., Soc. Expl. Geophys., Expanded Abstracts, 391–394.

Schoenberg, M., and Muir, F., 1989, A calculus for finely layered anisotropic media: *Geophysics*, **54**, 581–589.